Available online at www.sciencedirect.com
ScienceDirect
Geochimica et Cosmochimica Acta 71 (2007) 5985–6001
Geochimica et Cosmochimica Acta
www.elsevier.com/locate/gca

Gold deposition on pyrite and the common sulfide minerals: An STM/STS and SR-XPS study of surface reactions and Au nanoparticles

Yuri L. Mikhlin *, Alexander S. Romanchenko

Institute of Chemistry and Chemical Technology SB RAS, K. Marx Str., 42, Krasnoyarsk 660049, Russia

Received 9 April 2007; accepted in revised form 2 October 2007; available online 12 October 2007

Abstract

Gold species spontaneously deposited on pyrite and chalcopyrite, pyrrhotite, galena, sphalerite from $HAuCl_4$ solutions at room temperature, as well as the state of the reacted mineral surfaces have been characterized using synchrotron radiation X-ray photoelectron spectroscopy (SR-XPS), scanning tunneling microscopy and tunneling spectroscopy (STM/STS). The deposition of silver from 10^{-4} M $AgNO_3$ has been examined for comparison. Gold precipitates as metallic nanoparticles (NPs) from about 3 nm to 30 nm in diameter, which tends to aggregate forming larger particles, especially on pyrite. The Au 4f binding energies increase up to 1 eV with decreasing size of individual Au^0 NPs, probably due to the temporal charging in the final state. Concurrently, a positive correlation between the tunneling current and the particle size was found in STS. Both these size effects were observed for unusually large, up to 20 nm Au particles. In contrast, silver deposited on the minerals as nanoparticles of semiconducting sulfide showed no shifts of photoelectron lines and different tunneling spectra.

The quantity of gold deposited on pyrite and other minerals increased with time; it was lower for fracture surfaces and it grew if minerals were moderately pre-oxidized, while the preliminary leaching in Fe(III)-bearing media inhibited the following Au deposition. After the contact of polished minerals with 10^{-4} M $AuCl_4^-$ solution (pH 1.5) for 10 min, the gold uptake changed in the order $CuFeS_2 > ZnS > PbS > FeAsS > FeS_2 > Fe_7S_8$. It was noticed that the open circuit (mixed) potentials of the minerals varied in approximately the same order, excepting chalcopyrite. We concluded that the potentials of minerals were largely determined by Fe(II)/Fe(III) couple, whereas the reduction of gold complexes had a minor effect. As a result, the deposition of gold, although it proceeded via the electrochemical mechanism, increased with decreasing potential. This suggests, in particular, that the accumulation of "invisible" gold in arsenian pyrites and arsenopyrite under hydrothermal conditions may be explained by the low electrochemical potentials but not structural relationships between As and Au in solids.

1. INTRODUCTION

Gold is often associated with sulfide minerals (arsenopyrite, pyrite, chalcopyrite, pyrrhotite, galena) as "invisible" gold that is thought to consist either of submicrometer metallic particles or to be bound to sulfur in metal sulfide lattice (Cook and Chryssoulis, 1990; Friedl et al., 1995; Fleet and Mumin, 1997; Genkin et al., 1998; Cabri et al., 2000). Pyrite is one of the major minerals accumulating gold in most ores, although a solubility of Au in nonarsenian pyrite is minor (Cook and Chryssoulis, 1990; Tauson, 1998, 1999), and increased concentrations of gold are associated with arsenic content and iron deficiency (Fleet and Mumin, 1997; den Besten et al., 1999; Reich et al., 2005). The state and properties of both elemental and chemically bound gold as well as reaction mechanisms of the gold deposition are far from being completely understood.

A number of studies suggest a role of surface reduction and/or adsorption in the precipitation of gold in ore-depositing hydrothermal systems (Mycroft et al., 1995; Tauson et al., 1996, 1998; Scaini et al., 1997; Tauson, 1999; Simon

* Corresponding author.
E-mail address: yumikh@icct.ru (Y.L. Mikhlin).

0016-7037/$ - see front matter
doi:10.1016/j.gca.2007.10.001

et al., 1999a,b; Widler and Seward, 2002). Jean and Bancroft (1985), Hyland and Bancroft (1989), Mycroft et al. (1995), Maddox et al. (1998), Scaini et al. (1997, 1998), Widler and Seward (2002) have studied the deposition of gold from aqueous solutions on pyrite and other minerals using X-ray photoelectron spectroscopy (XPS), scanning electron microscopy (SEM), electrochemical and other techniques. Mycroft et al. (1995) have found 50–100 nm Au spheres containing progressively smaller spheres at pyrite reacted in $AuCl_4^-$ solutions (e.g., 1.9×10^{-3} M for 15 min). The Au clusters tend to be found in association with either microcracks or pits on the pyrite surface, and with "haloes" around the clusters. The Au 4f XPS spectra were typically fitted with three peaks attributed to metallic gold, gold nanoparticles (Au NPs), with the binding energy being a function of Au particle size, and minor Au(I) species. The authors have suggested that the gold nanoparticles are composed of less than 100 atoms which cannot be detected by SEM. Maddox et al. (1998) have reported that about 300 nm Au particles deposit on pyrite contacted with a solution of 10^{-4} M $KAuCl_4 + 1$ M KCl (pH 3) for 10 min, whereas Au NPs less than 50 nm in size form on arsenopyrite; the total amount of gold on arsenopyrite was about seven times larger than that on pyrite. It has been concluded that the rate-limiting step in the deposition of gold on pyrite is the reduction of Au(III) to Au(I), whereas the rate of reduction of gold on arsenopyrite is controlled significantly by the rate of oxidation of arsenopyrite. Heasman et al. (2003) have determined by transmission electron microscopy (TEM) that individual gold clusters are between 2.9 and 7.7 nm in diameter and they may form composite clusters up to 500 nm over the reduction of aqueous Au(III) on pyrite, green rust, and chalcopyrite. Recently, Palenik et al. (2004) and Reich et al. (2005) have revealed discrete 5–10 nm gold nanoparticles in As-rich overgrowths on pyrite from a Carlin-type deposit by using analytical and high-resolution TEM. Reich et al. (2005) have found a maximum Au/As molar ratio of 0.02 in arsenian pyrites, with the gold above this solubility limit occurring as native Au^0.

Scanning probe microscopy (SPM), which can provide resolution better than 1 nm along with additional information beyond the imagining, has been employed to examine the experimental deposition of gold in few studies on galena (Eggleston and Hochella, 1991, 1993; Becker et al., 1997), copper sulfides $Cu_{2-x}S$ (Barzyk et al., 2002), and arsenopyrite (Mikhlin et al., 2006a). Eggleston and Hochella (1991, 1993) have found by scanning tunneling microscopy (STM) that gold islands are about 100 nm long and 10 nm wide on fresh fracture PbS surfaces and hemispherical (5–10 nm in diameter) on pre-oxidized galena after its contact with a solution of 1 ppm $KAuCl_4 + 1.1$ M NaCl (pH 3.2) at 25 °C for 1.5 h. The metallic gold showing a uniform density of states near the Fermi level and semiconducting galena were discriminated by using of tunneling spectroscopy (STS). Mikhlin et al. (2006a) have characterized arsenopyrite samples oxidized in gold(III) chloride solutions at ambient temperatures by atomic force microscopy (AFM), STM/STS, and XPS. Exposure of arsenopyrite to 10^{-5}–10^{-3} M $AuCl_4^-$ solutions results in the deposition of 8–50 nm gold particles, with only a small fraction of the gold being present as Au(I)–S species. The moderate oxidation (e.g., ageing of arsenopyrite in air) promotes the subsequent gold deposition; in contrast, the amount of surface Au sharply reduces after arsenopyrite has been preliminary leached in ferric chloride and ferric sulfate solutions. A reduction of the tunneling currents with decreasing the Au^0 particle size was observed in STS. This effect was tentatively ascribed to hindering the electron transitions by electrostatic charge emerging on gold nanoparticles (Coulomb blockade), and a positive shift of the Au 4f band was explained by the final state effect originating from the photohole remaining on the Au NPs.

Pyrite surfaces generated by cleaving in air (Eggleston and Hochella, 1992) and in ultra high vacuum (Rosso et al., 1999, 2000) have been investigated using STM/STS with the emphasis on the atomic and electronic structure and defects. Eggleston et al. (1996) have found that initial oxidation of pyrite in air proceeds via the growth of nanometer-scale oxidized patches containing Fe(III) instead of Fe(II). Similar results have been reported by Rosso et al. (1999) for pyrite reacted with oxygen and water in vacuum. In general, there is a considerable literature on the oxidation of pyrite under various conditions (see Rimstidt and Vaughan (2003), Descostes et al. (2004), Rosso and Vaughan (2006a,b) for a survey), but the reaction mechanisms have not been fully clarified. To our knowledge, SPM techniques were not used to explore gold-bearing pyrites, either synthetic or natural, up to now.

In the present study, we applied STM/STS, AFM, and synchrotron radiation based XPS (SR-XPS) to investigate the deposition of gold on pyrite in comparison with other metal sulfides and with the deposition of silver. The research was performed using rather high concentrations of gold (III) chloride at ambient temperature for ease of experiment. The aim was to gain further insight into the mechanisms of surface reactions and specific properties of precipitated gold nanoparticles, which are expected to arise from the size effects and can play an important role in the behaviour of "invisible" gold. This information is necessary also to develop SPM-based methods able to find "invisible" gold in natural materials.

2. EXPERIMENTAL

2.1. Materials and sample preparation

Research grade pyrite crystals (without inclusions of foreign phases, pores and other visible defects) were from Ozernoye, Russia, they had an average composition of $FeS_{2.0}$ and contained Cu 0.14, Si 1.03, Zn 0.11, Ca 0.19, and As less than 0.05 wt% as impurities determined by X-ray fluorescence analysis. Natural polycrystalline chalcopyrite, monoclinic pyrrhotite, sphalerite and single crystals of galena were described in detail elsewhere (Mikhlin et al., 2004a,b; Mikhlin and Tomashevich, 2005; Mikhlin et al., 2006b). Samples were cut and polished at silicon carbide paper; the polished surfaces were cleaned by wet filter paper to remove fine particles before a chemical treatment. Some specimens were fractured in air just before microscopic or

spectroscopic studies or conditioning in aqueous solutions. For electrochemical experiments, a copper layer was electrochemically formed on one sample face, tinned copper wire was soldered to the Cu coating, and the specimens were embedded in Teflon, with the working face exposed.

Gold was deposited on pyrite from unstirred 10^{-5}–10^{-3} M solutions of $HAuCl_4$ (commonly 10^{-4} M at pH 1.5 or 3) at 20 ± 1 °C. The reacted samples were quickly rinsed with water before examination. All the solutions were prepared from reagent grade chemicals and doubly distilled water; no attempt was made to prevent ingress of air. Necessary precautions against (photo)decomposition of the gold solutions during their storing were undertaken, but the reactions vessels were uncovered to room lights as this do not affect the gold deposition (Hyland and Bancroft, 1989; Mycroft et al., 1995). Some deposition experiments were conducted with pyrite polarized previously during a potential sweep going from the rest potential to a predetermined potential value at 20 ± 1 °C or with samples treated by 1 M HCl + 0.4 M $FeCl_3$ or 0.5 M H_2SO_4 + 0.2 M $Fe_2(SO_4)_3$ media without stirring at 50 ± 1 °C. Then the samples were rinsed with distilled water in order to remove remaining electrolyte, and placed into an Au-bearing solution or examined by ex situ XPS and SPM as described below. A potentiostat PI-50-1 equipped with a programmer PR-8 (ZIP, Belarus) and a conventional three-compartment glass cell were used in the electrochemical experiments. Counter and reference electrodes were Pt wire and saturated Ag/AgCl electrode, respectively; all potentials are given with respect to the latter. Pyrrhotite, chalcopyrite, galena were treated in the same way.

2.2. Microscopic studies

AFM, STM and STS investigations were performed in air using a multimode Solver P47 device (NT-MDT, Russia) equipped with a 14 μm scanner. The AFM experiments were conducted using mainly ex situ tapping mode (TM-AFM), with simultaneous height and phase image recording. Typical force constant of the silicon cantilever was 6 N/m. No less than 3 points at each of at least 3–4 mineral samples treated in parallel were imaged. The probe used in STM/STS measurements was a mechanically cut 90% Pt–10% Ir wire; positive bias was defined as a positive voltage on the sample with respect to the tip. AFM and STM images were collected at the scan rate of 1–2 Hz with 256 or 512 lines per scan; no smoothing procedure was applied. The I–V curves were measured using a fixed tip-sample separation by breaking the feedback circuit for a few microseconds at a desired surface location. All curves shown in this article represent the average character of 5–10 reproducible measurements without changing the lateral position, the tip–sample distance and the potential sweep rate. Scanning electron microscopy characterization and energy dispersive X-ray analysis (EDX) were carried out using a JSM-6700F instrument (Jeol).

2.3. SR-XPS and XANES

The XPS spectra were measured at the dipole magnet beamline of the Russian–German laboratory (Fedoseenko et al., 2003) at the synchrotron radiation storage ring BESSY II (Berlin, Germany) at pressure of $\sim 10^{-8}$ Pa and room temperature. The excitation energy was usually 1000 eV, unless otherwise stated; the pass energy of a VG-CLAM 4 analyzer was 20 eV for the narrow scans. Binding energies were corrected for electrostatic charge using the C 1s peak (285.0 eV). A value of 83.6 ± 0.05 eV was obtained for the Au $4f_{7/2}$ peak of metallic gold plate in our experiments (the binding energy of 83.72 eV was documented in the course of the device calibration). Atomic ratios of elements were calculated from integrated peak areas corrected for the experimental photo-ionization cross sections (Briggs and Seah, 1992). The spectra were fitted using a convolution of Gaussian and Lorenzian peak shapes after subtracting a nonlinear Shirley background; the spectra shown in the Figures below were normalized in height. X-ray absorption spectra (Fe $L_{2,3}$, Cu $L_{2,3}$, S $L_{2,3}$, and O K XANES) were recorded in the total electron yield (TEY) mode; the transmission of the monochromator was accounted for by measuring the TEY of polycrystalline Au plate.

3. RESULTS

3.1. Original and oxidized pyrite surfaces

The results obtained in this research were not face specific, because pyrite crystals did not have a well-developed direction of cleavage, and the surfaces obtained by cleaving parallel, for example, to a {1 0 0} plane were composed of a combination of {1 0 0} terraces, other crystal faces, and a conchoidal fracture (Rosso et al., 1999). Fig. 1a and b illustrate some STM images of the surfaces exhibiting a topography inhomogeneity in submicrometer and nanometer scales. After polishing or prolonged aging of pyrite in air, the reaction products in the shape of nano- and submicrometer scale islands are seen in AFM (Fig. 1c) but not in STM images.

Images collected on samples leached by acidic solutions of ferric chloride or ferric sulfate at elevated temperatures show the development of etch pits and the islands of oxidation products about 20–100 nm in lateral dimensions (Electronic Annex, Fig. EA-1). As the leaching progresses, the surface of pyrite becomes increasingly disordered, whereas the amount of surface substances discernible in the AFM phase images grows slowly. The roughness in nanometer and submicrometer scale observed also in STM is mainly due to non-uniform dissolution of pyrite phase; such structures are typical for leached metal sulfides (De Guidici and Zuddas, 2001; De Guidici et al., 2002; Mikhlin et al., 2006a,b).

Fig. 2 shows photoelectron S 2p spectra acquired from pyrite samples. It should be mentioned that there are a number of detailed studies of pyrite surfaces, including related to the gold deposition (Mycroft et al., 1995; Maddox et al., 1998; Scaini et al., 1997, 1998; Widler and Seward, 2002), SR-assisted XPS (Schaufuss et al., 1998a,b; Elsetinow et al., 2000; Nesbitt et al., 2000; Uhlig et al., 2001; Leiro et al., 2003; Kendelewicz et al., 2004), and XANES (Hallmeier et al., 2002; Todd et al., 2003). Our primary

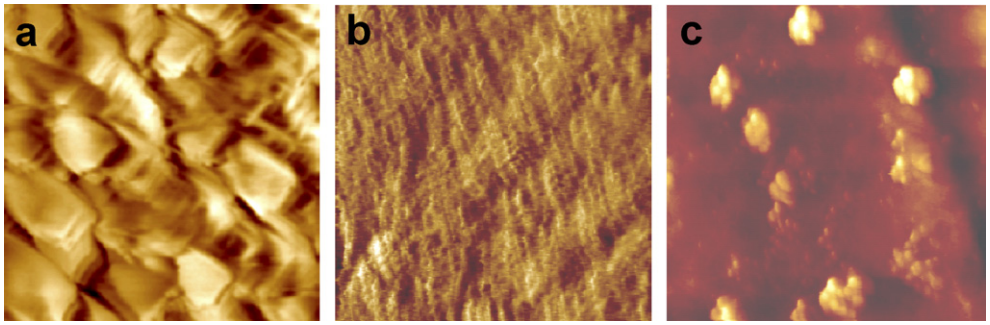

Fig. 1. STM images (a and b) of two fractured pyrite surfaces ($I_{SP} = 0.6$ nA, $V = 0.1$ V); image sizes are 1×1 μm and 0.5×0.5 μm, Z range is 42 nm and 25 nm, respectively. (c) Tapping mode AFM image of pyrite polished in air; image size is 5×5 μm, Z range is 0.40 μm.

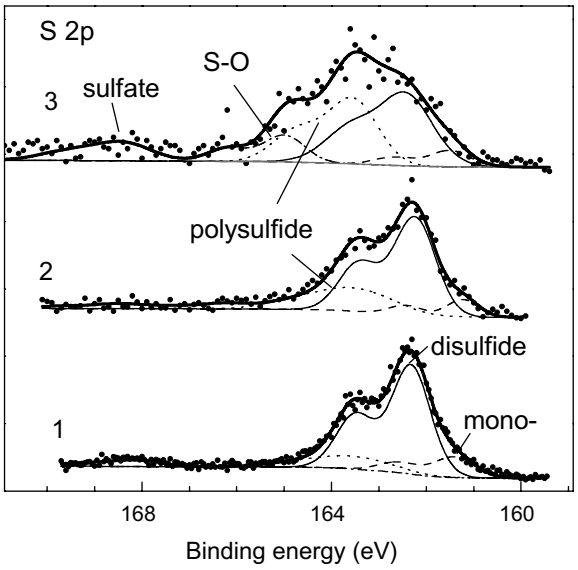

Fig. 2. S 2p spectra of pyrite specimens (1) fractured in air, (2) polished in air and (3) leached in 0.5 M $H_2SO_4 + 0.2$ M $Fe_2(SO_4)_3$ solution at 50 °C for 1 h.

aim was to compare the surfaces of pyrite before and after the gold deposition with the ones of other sulfide minerals, so only selected photoelectron spectra and their brief discussion are given for the sake of briefness. The S 2p spectra of pyrite contain the main peak at binding energy of 162.3 eV and two weaker components at 161.3 eV and 163.5 eV, which can be ascribed to dimers S_2^{2-}, monosulfide and polysulfide species, respectively (Nesbitt et al., 1998, 2000; Elsetinow et al., 2000). The intensity of the polysulfide signal increases to some extent for the sample polished in air, and it grows considerably after the oxidative leaching of pyrite, indicating the depletion of the surface layer in iron. The small peak at 165 eV is likely to arise from an intermediate oxysulfur species (Schaufuss et al., 1998a,b). The corresponding Fe 2p spectra will be present later in Fig. 11.

Galena, pyrrhotite, and chalcopyrite specimens were described in detail elsewhere (Mikhlin et al., 2004a,b, 2006b; Mikhlin and Tomashevich, 2005).

3.2. Deposition of gold

3.2.1. Microscopic analysis

3.2.1.1. Pyrite. SEM micrographs of the pyrite samples polished and then reacted in 10^{-4} M $HAuCl_4$ show Au particles of approximately 10 nm in diameter after 2 min of exposure; both the size and amount of the particles increase with time, some of them reaching 50–200 nm in the lateral dimension (Fig. 3a and b). AFM and especially STM provide much more details. Tapping mode AFM (Fig. EA-2) reveals a number of islands as large as about 500 nm, which seem to consist of the products of pyrite oxidation, along with plentiful particles of 10–20 nm in size, attributable mainly to metallic gold. However, TM-AFM appears to overestimate the size of the smaller particles, and it has insufficient resolution to detect NPs as small as several nanometers. In turn, the STM images of the reacted surfaces are distorted because nonconducting substances are missed; at the same time, this allows distinguishing gold species among other products even at rough substrates. The gold nanoparticles seen in the STM images (Fig. 4a–e) are usually slightly elongated; they are about 10 nm long in the initial stages of the deposition and tend to associate with each other. The gold aggregates grow to 50 nm and further, and many of them are clearly composed of 10–20 nm clusters, which in turn may consist of even lesser ones (Fig. 4c). The clusters become more densely packed with the inner borders indiscernible with time of reaction.

Oxidation of pyrite before its interaction with Au(III) solutions effects both quantity and morphology of gold particles. For a fresh fracture surface, the number of Au NPs produced by the gold deposition for 10 min is essentially lower than in the case of polished samples. The size of individual gold clusters increases to about 20 nm and more, while the number of the particles first grows and then decreases as the preliminary oxidation of pyrite has advanced, in particular, if pyrite has been leached in the ferric sulfate solution or pre-oxidized electrochemically (Fig. 4e and f).

We kept in mind that very small gold nanoclusters may be brushed away by a probe, remaining invisible in STM (see, for example, Lopez-Salido et al., 2006), and tried to find them by varying setpoint current, voltage, rate of scanning, etc. Only a minor number of 3–5 nm particles were usually detected (Fig. 4), but, in rare cases, arrays of such

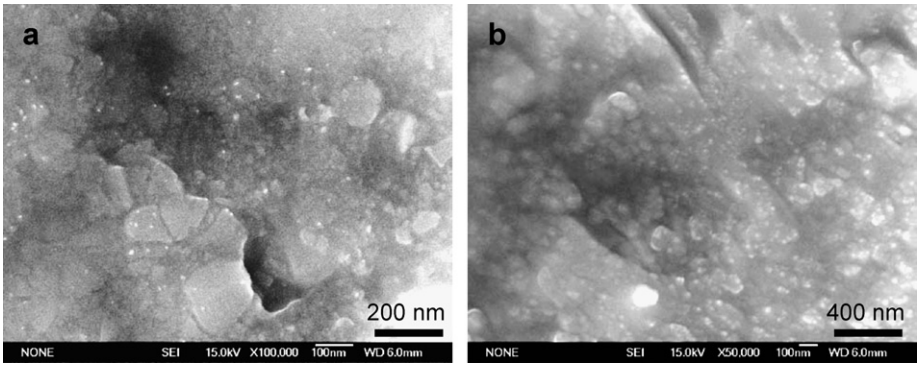

Fig. 3. SEM images of polished pyrite after deposition of gold from 10^{-4} M $AuCl_4^-$ solution (a) for 2 min and (b) 10 min.

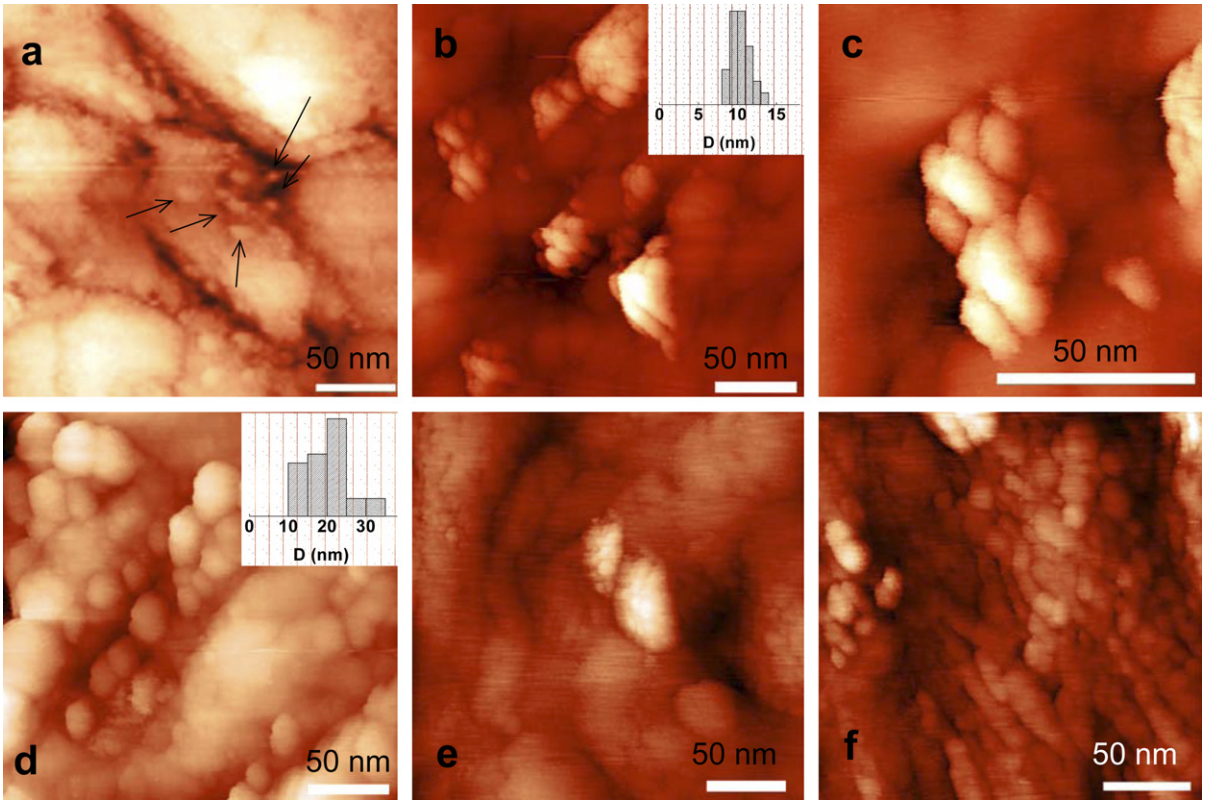

Fig. 4. Representative STM images of gold nanoparticles deposited onto polished pyrite from 10^{-4} M $HAuCl_4$ solutions at 20 °C (a) during 2 min (arrows point at some of about 10 nm Au NPs), (b and c) 10 min, (d) 30 min. (e) Pyrite pre-oxidized in 0.5 M H_2SO_4 + 0.2 M $Fe_2(SO_4)_3$ solution at 50 °C for 1 h and (f) anodized in the potential sweep (5 mV/s) to 1.1 V and then contacted with the gold solution for 10 min and 5 min, respectively.

nanoparticles were observed on some spots, possibly due to an accidental local decomposition of intermediate gold(I) complexes. It will be demonstrated below that the STM, STS and XPS data for pyrite and other minerals are consistent with characteristics of the "visible to STM" nanoparticles described above, so it is unlikely that Au NPs less than 4–5 nm are actually widespread. At the same time, STM may overestimate the real size of the nanoparticles by 20–50%, in particular, due to their mobility.

Both STM and AFM revealed nanoscale inhomogeneity of the surfaces arising due to the oxidation of pyrite. Gold islands were sometimes close to etch pits, suggesting a very small spatial separation between the locations of the coupled reactions of anodic dissolution of pyrite and cathodic reduction of gold, but generally neither etch pits or haloes, observed by Mycroft et al. (1995), nor other reaction products were definitely associated with gold.

3.2.1.2. Other minerals. The interaction of galena with aqueous $AuCl_4^-$ complexes results first in individual particles from 1–3 nm to 10–15 nm in diameter, which are seen, together with numerous nanoscale etch pits, in the STM

images (Fig. 5a). Under conditions standard for this study (10^{-4} M $AuCl_4^-$, 20 °C, 10 min), a large part of the substrate is covered with quite uniform spherical metal nanoparticles of 3–10 nm in diameter, leaving almost bare PbS spots up to several hundred nm in size (Fig. 5b). AFM images having lower resolution depict such surfaces as a nanostructured gold film with holes (uncovered PbS) and protrusions above the film. The protrusions are composed of either gold particles, mainly shifted by the probe, or oxidation products (elemental sulphur, etc.), which can be differentiated in the phase image (Fig. EA-3). The reaction is commonly accepted to proceed via the electrochemical mechanism (Sakharova et al., 1975; Maddox et al., 1998), and one can speculate that the anodic oxidation of PbS took place on the naked PbS regions and Au NPs deposited on the cathodic areas occupying the major part of the surface.

Gold nanoparticles precipitated under the same conditions on chalcopyrite are bigger than on galena; their size varies from 5 to 30 nm, with the average of about 11 nm (Fig. 5c and d). It is important to note that many of the particles contact each other. If chalcopyrite has been oxidized in ferric sulfate or ferric chloride solutions before the deposition of gold, the quantity of Au NPs of about the same size sharply decreased, and they were mostly isolated.

A much lower amount of Au NPs of about 8 nm in average diameter, isolated or arranged in composite islands in about equal parts, were observed on polished pyrrhotite (Fig. 5e and f). However, gold NPs cover a substantial part of the surface of pyrrhotite leached previously in 1 M HCl or 0.5 M H_2SO_4 under non-oxidative conditions. The pretreatment in Fe(III) containing solutions had a small effect on the following gold deposition (not in Figures).

3.2.2. Tunneling spectra

The area-averaged tunneling *I–V* spectra of initial pyrite (Fig. 6a) show a conductance gap that is less than the band gap of bulk pyrite (about 1 eV, Eyert et al., 1998), probably due to a high density of surface states in the band gap (Eggleston et al., 1996; Rosso et al., 1999). The gap becomes apparently narrower after pyrite has been leached by the Fe(III) solutions, indicating either a substantial increase in the density of surface states or fundamental changes in the electronic structure of the oxidized, iron-deficient surface layer. Earlier (Mikhlin, 2000; Mikhlin et al., 2004b, 2006a,b), we proposed to consider such reacted layers akin to disordered or glassy chalcogenide semiconductors (Mott and Davis, 1979; Tsendin, 1996). According to this approach, the gap states may originate from the localized band tails arising due to potential fluctuations, as well as from specific defects. Localization of states in the upper portion of the valence band caused by the disordering is thought to be responsible for low mobility of the charge carriers and hence the passivity of metal sulfides upon oxidation.

Fig. 6a–d shows also the representative current–voltage curves measured above gold nanoparticles on pyrite and other metal sulfides. The curves related to silver-containing particles are given too and considered in Section 3.3. The current passing through presumably metallic gold particles is lower than that for bare surfaces of the semiconducting minerals, except near the Fermi level (zero bias). The electron tunneling increases as the nanoparticles grow or become aggregated; for dense gold films formed as a result of a large Au uptake, the curves approach those for the bulk metal. Similar correlations were observed for all minerals, despite different experimental parameters (setpoint current, bias voltage, and, hence, sample–tip distance). Such a behaviour found for 5–20 nm gold particles deposited on arsenopyrite (Mikhlin et al., 2006a) was tentatively explained in terms of Coulomb blockade effects typical for ultrafine gold particles (Han et al., 1998; Daniel and Astruc, 2004). This means that the electric charge of the particle having a very small capacitance retards electron transfer in a particle–tip junction; a layer with a high impedance should also exist underneath the particle. It must be emphasized that Coulomb blockade has been usually observed at essentially smaller gold particles, although the effect is, in principle, possible for Au NPs less than 20 nm in diameter at room temperature (Han et al., 1998; Ohgi and Fujita, 2003). The interface between gold nanoparticles and oxidized metal sulfides has a complex and poorly explored structure, and other reasons for the suppression of electron tunneling cannot be ruled out, including that electric conductivity across small metal–semiconductor contacts depends on their areas.

3.2.3. XPS analysis

3.2.3.1. Gold. Fig. 7 represents the Au $4f_{7/2,5/2}$ doublet spectra from several pyrite samples reacted in the gold containing media. The bands have different energy positions, widths and are often asymmetric due to contributions from several gold species, so the Au $4f_{7/2}$ lines are better fitted with two or three maxima. A component at a binding energy approaching 83.6 eV can be assigned to metallic gold; its relative intensity correlates qualitatively with a share of gold particles larger than 15–20 nm and dense aggregates observed in STM. A line at 85–85.5 eV that corresponds to chemically bonded gold(I), most likely Au(I)–S species (Scaini et al., 1998), reaches at most 20% of the total intensity when the gold uptake is small. This is the case, in particular, for pyrite reacted in 10^{-4} M $HAuCl_4$ solution for 2 min. The peaks shifted by less than 1 eV toward higher binding energies relative to the bulk metal can be attributed to Au^0 nanoparticles (Scaini et al., 1998; Tanaka et al., 2003; Boyen et al., 2005; Compagnini et al., 2006; Mikhlin et al., 2006a). The positive binding energy shift gradually decreases with increasing the time of reaction and the quantity of precipitated gold, but it stays small for strongly preoxidized surfaces, probably due to the formation of comparably large Au particles (Fig. 4e and f).

The same tendencies were found for gold precipitated on other minerals (Fig. 8). The Au 4f spectra from pyrrhotite and, to a certain degree, chalcopyrite specimens are rather wide, indicating a presence of "bulk" metal along with ultrasmall Au NPs. The very broad Au 4f line observed for sphalerite could be well fitted with similar components; alternatively, the large band width can be explained in terms of spatially non-uniform electrostatic charging of this

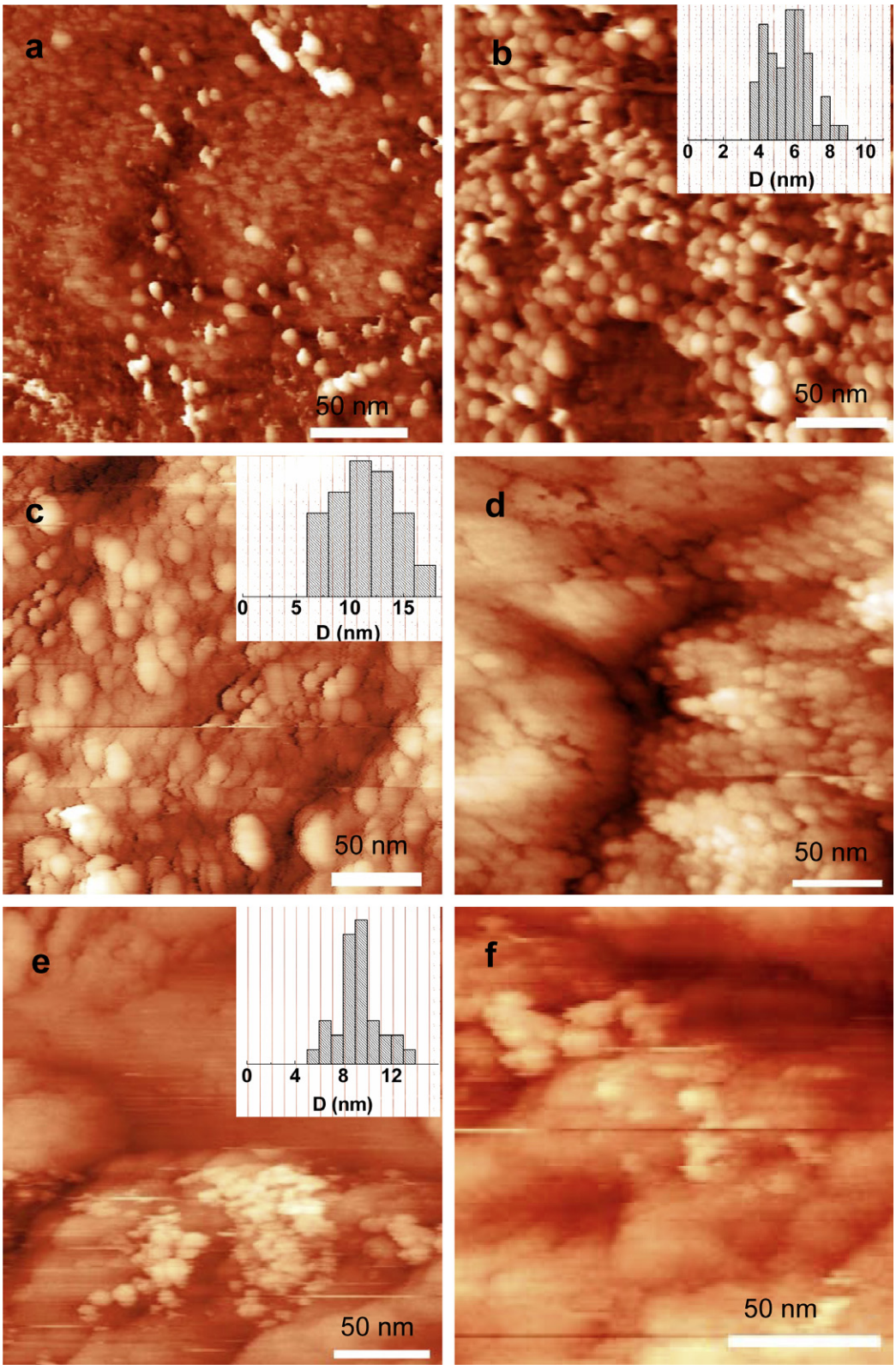

Fig. 5. STM images of (a) galena surfaces reacted with 10^{-5} M $HAuCl_4$ for 30 min and (b) with 10^{-4} M $HAuCl_4$ solutions for 10 min (I_{SP} = 0.1 nA, $V_B = -0.1$ V), (c and d) chalcopyrite (I_{SP} = 0.1 nA, $V_B = -0.1$ V) and (e and f) monoclinic pyrrhotite ($I_{SP} = 0.2$ nA, $V_B = -0.4$ V) treated by 10^{-4} M $HAuCl_4$ solutions for 10 min.

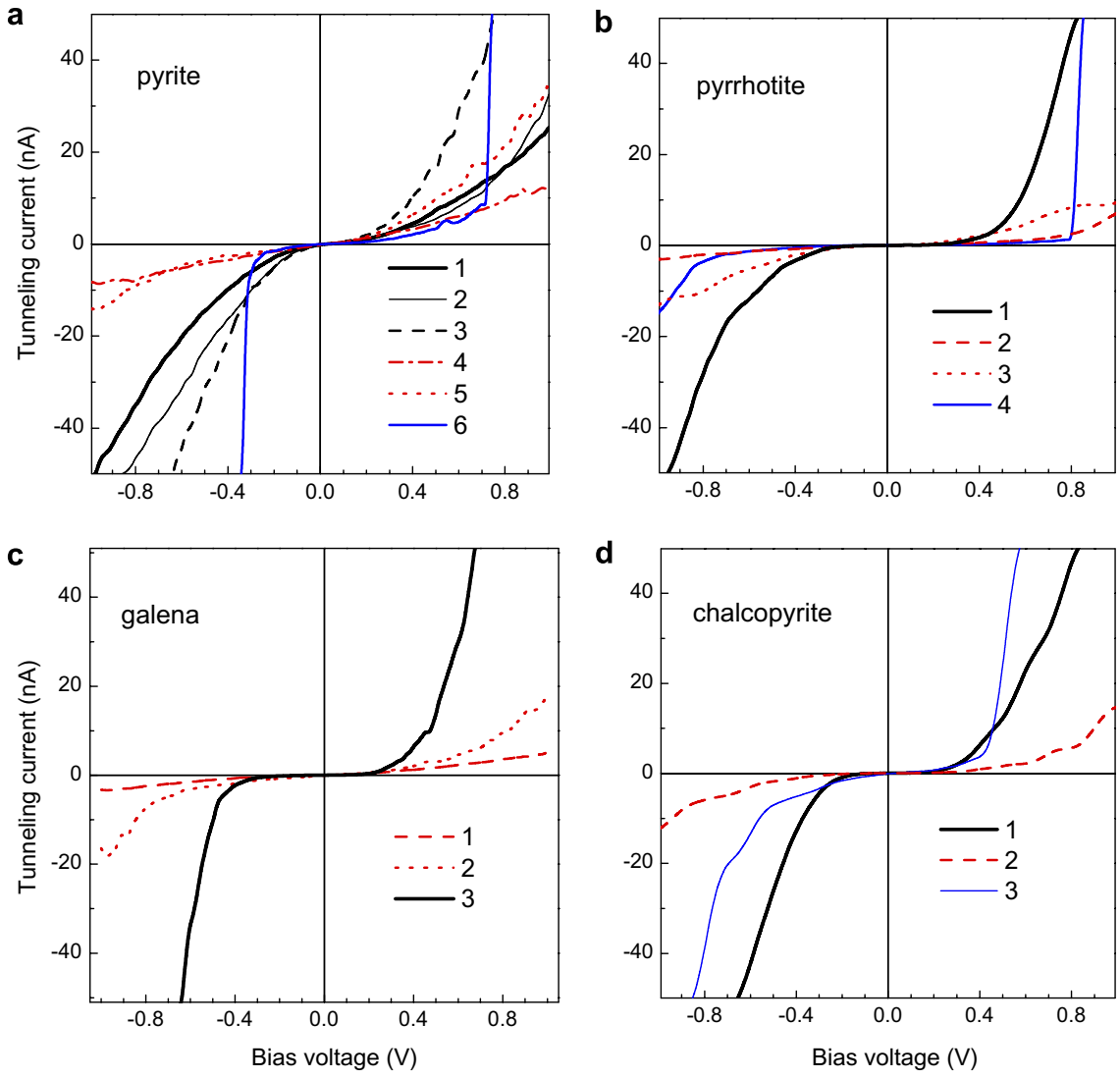

Fig. 6. Tunneling spectra collected from (a) pyrite above (1) fractured in air, (2) aged in air for 10 days after the cleavage, (3) leached in 0.5 M $H_2SO_4 + 0.2$ M $Fe_2(SO_4)_3$ at 50 °C for 1 h, (4) above ~12 nm Au^0 particle, (5) about 30 nm aggregate of Au NPs, (6) Ag-containing protrusion. $I_{SP} = 0.6$ nA, $V_B = 0.1$ V. (b) Monoclinic pyrrhotite (1) polished, (2) about 8 nm Au NP, (3) aggregate of Au NPs, (4) an 20 nm Ag-bearing NP. $I_{SP} = 0.2$ nA, $V_B = 0.1$ V. (c) Galena samples reacted in 10^{-4} M $HAuCl_4$ for 10 min (1) a separated ~5 nm Au^0 particle, (2) a dense film formed by Au nanoparticles, and (3) bare PbS surface. $I_{SP} = 0.1$ nA, $V_B = -0.1$ V. (d) Chalcopyrite (1) polished, (2) 10 nm Au NP, (3) 20 nm Ag-bearing particle. $I_{SP} = 0.1$ nA, $V_B = 0.1$ V.

wide gap semiconductor, although Zn $2p_{3/2}$ and S 2p lines (not shown) were comparably narrow. In contrast, the Au 4f peaks for gold on galena are rather narrow and shifted by almost 1 eV, in agreement with the size distribution of Au NPs (Fig. 5b). Generally, the binding energy decreases with increasing the size of Au nanoparticles determined by STM for all minerals studied, with the effect disappearing for Au particles larger than about 15 nm and for the ones amalgamated or densely packed. The dimension of individual Au NPs seems to play the main role while that of aggregates composed of the smaller clusters is of minor importance. Such a shift of the Au 4f peaks as a function of Au^0 cluster size can be induced by Coulomb interactions of the particle positively charged during the escape of the photoelectron, thereby reducing its kinetic energy (and so increasing apparent binding energy). However, the effect normally decreases to less than 0.1–0.2 eV for clusters larger than 3 nm in diameter (Boyen et al., 2005; Compagnini et al., 2006). Aside from this final-state effect, the binding energy may change due to such initial state effects as a charge transfer between the nanoparticle and the support (for example, Okazawa et al., 2006), a presence of adsorbates (Tanaka, 2003; Daniel and Astruc, 2004), or shorter bond distances in small clusters than in bulk metals (Richter et al., 2004) but again they take place for the clusters less than 3–4 nm. Moreover, a clear albeit qualitative correlation between the Au 4f peak shifts and the suppression of tunneling currents observed for pyrite and other minerals seem to corroborate the essentially electrostatic nature of these phenomena.

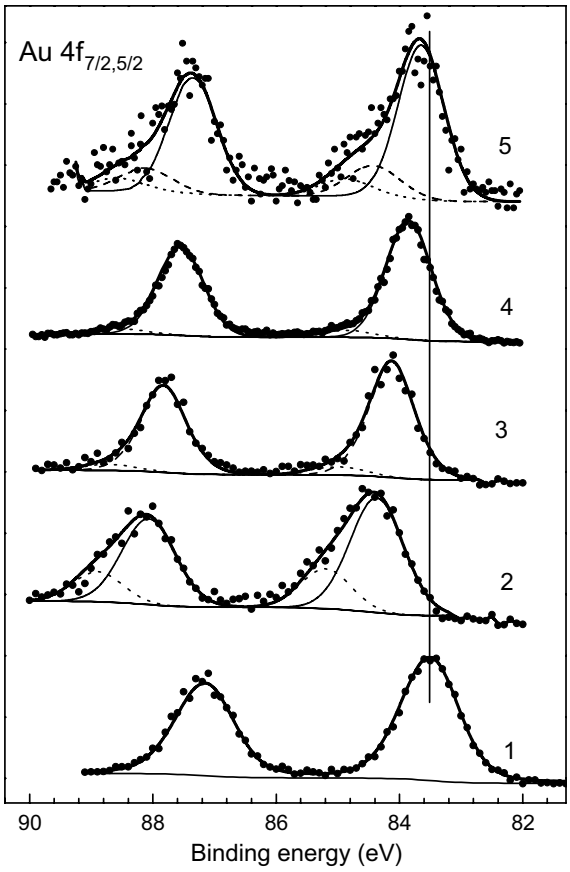

Fig. 7. Au 4f photoelectron spectra from (1) polycrystalline gold plate, polished pyrite reacted with 10^{-4} M $HAuCl_4$ solution for (2) 2 min, (3) 10 min, (4) 30 min, and (5) pyrite anodized in the potential sweep to 1.1 V before the gold deposition for 5 min.

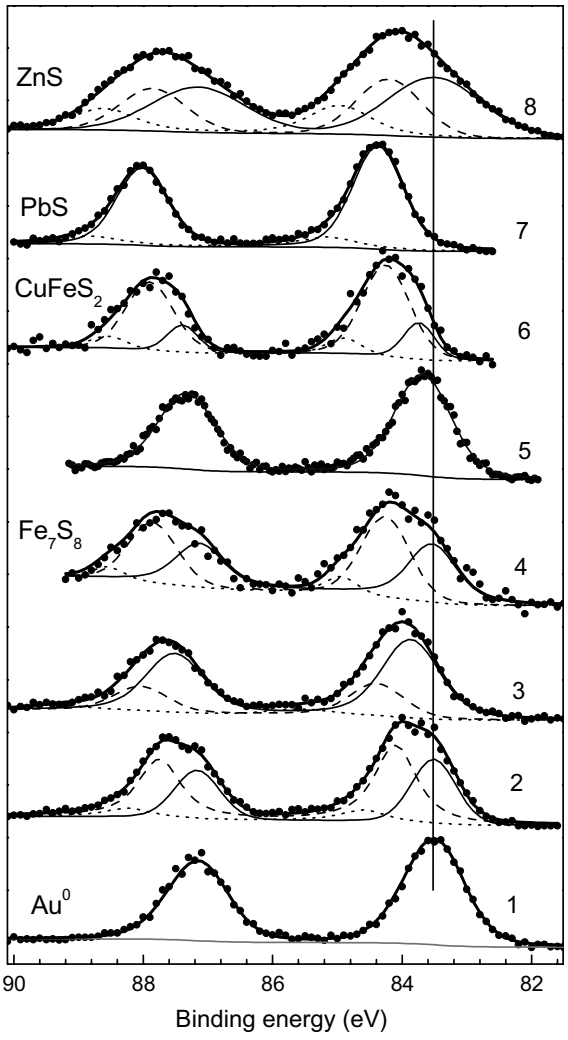

Fig. 8. Au 4f spectra from (1) polycrystalline gold and gold deposited from 10^{-4} M $HAuCl_4$ solution during 10 min on (2) polished pyrrhotite, (3) pyrrhotite treated in 0.5 M H_2SO_4 and (4) 0.5 M H_2SO_4 + 0.2 M $Fe_2(SO_4)_3$ solutions (50 °C, 30 min), chalcopyrite (5) polished and (6) leached in 1 M HCl + 0.4 M $FeCl_3$ solution (50 °C, 30 min), (7) galena, and (8) sphalerite.

3.2.3.2. Sulfur. The S 2p spectra from pyrite contacted with aqueous Au(III) ions (Fig. 9) show a slightly enhanced intensity near 163.5 eV binding energies that is commonly attributed to polysulfide (Scaini et al., 1997; Schaufuss et al., 1998a,b; Uhlig et al., 2001; Kendelewicz et al., 2004). During reaction, the intensity increases but remains far less than for pyrite leached in ferric iron containing solutions (Fig. 2). The signals from monosulfide ions (approximately 161 eV) become somewhat stronger too, but disulfide components at about 162 eV still predominate. The deposition of gold on the surfaces of pyrite pre-oxidized in Fe(III)-bearing media or anodized electrochemically results in further increasing intensity in the high binding energy region. X-ray absorption S L-edge spectra (Fig. EA-4) mostly agree with the above conclusions but they are indicative of higher concentrations of several S–O species as compared with XPS, probably due to higher surface sensitivity of TEY XANES.

The S 2p spectra from galena, chalcopyrite and, to a smaller extent, pyrrhotite are modified by the deposition of gold more deeply (Fig. 10). The spectra show strong signals from disulfide and polysulfide species at about 162 eV and 163.5 eV, denoting in fact the end and medial atoms in anions S_n^{2-}, $n \geqslant 2$, respectively (Termes et al., 1987; Mikhlin, 2000; Mikhlin et al., 2000). The unreacted minerals include only monosulfide ions, and S–S bonding occurs as a result of a depletion of the oxidized surface layers in metals. After the preliminary oxidative leaching in Fe(III)-bearing solutions that gives rise to the significant metal depletion, the proportion of the high-energy components enhances after the deposition of gold, indicating that the excess of sulfur in the metal-deficient layer further increases. It is possible also that sulfur forms a polysulfide-type covering on Au^0 (Vericat et al., 2004). Some sulfur atoms should be bonded to minor Au(I) species corresponding to the Au $4f_{7/2}$ component at about 85 eV, which occur either on Au nanoparticles or, more likely, on the surface of underlying minerals since the concentration of Au(I) decreases with an increase in the amount of deposited gold. Unfortunately, it was impossible to separate, including by varying the energy of excitation photons and using XANES, weak contributions from sulfur associated with

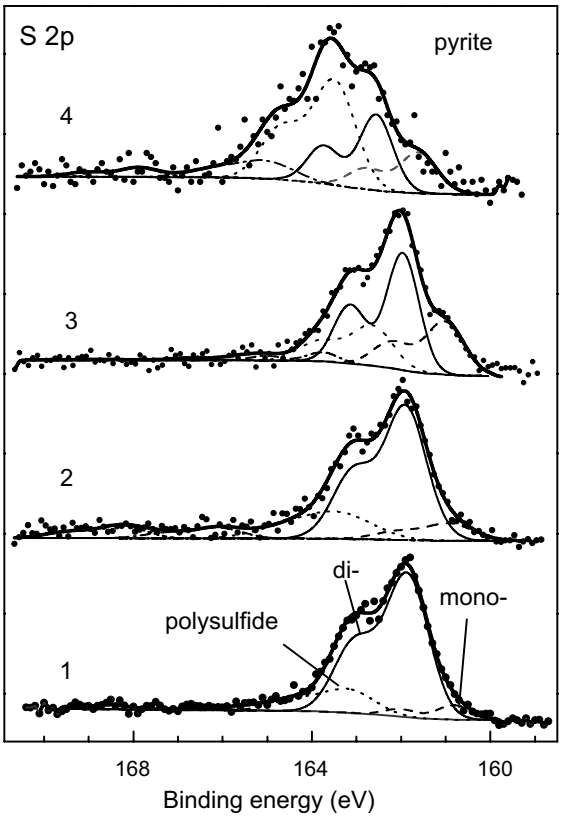

Fig. 9. S 2p spectra collected from pyrite samples reacted in 10^{-4} M $HAuCl_4$ for (1) 2 min, (2) 10 min, (3) 30 min, and (4) treated in 0.5 M H_2SO_4 + 0.2 M $Fe_2(SO_4)_3$ solution (50 °C, 30 min) before the gold reduction during 30 min.

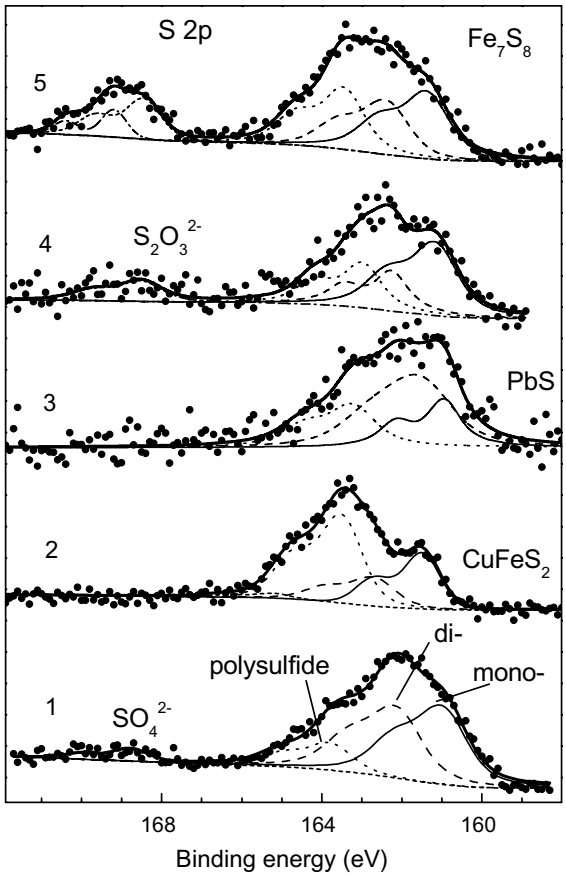

Fig. 10. S 2p spectra from minerals reacted in 10^{-4} M $HAuCl_4$ solutions for 10 min: chalcopyrite (1) polished, (2) treated in 1 M HCl + 0.4 M $FeCl_3$ solution (50 °C, 30 min), (3) galena, and pyrrhotite (4) polished and (5) leached in 0.5 M H_2SO_4 + 0.2 M $Fe_2(SO_4)_3$ solution (50 °C, 30 min) before the gold deposition.

Au because of much stronger signals from the reacted metal sulfides. Oxysulfur species were minor, and significant quantities of sulfate ions were found only after the preliminary ferric sulfate treatment, mainly due to sulfate adsorption.

3.2.3.3. Iron. The Fe 2p spectra of pyrite (Fig. 11) are dominated by a narrow peak at 707.3 eV originating from ferrous iron in a low-spin configuration; the spectra also contain minor contributions from high-spin Fe(II)–S, Fe(III)–S, and Fe(III)–O species as a high binding energy tail, which has been observed even for the vacuum fractured surfaces (Schaufuss et al., 1998a,b; Nesbitt et al., 1998, 2000). The tail is less pronounced for pyrite contacted with 10^{-4} M Au(III) solution at pH 1.5 than for the sample fractured in air, and it increases in intensity for the sample reacted with $AuCl_4^-$ at pH 3 and, especially, leached in acidic ferric sulfate solutions. Detailed analysis of these complex spectra containing several sets of multiplet components (Nesbitt et al., 2000 and references herein) and so the behaviour of pyritic iron is beyond the framework of the current article. It should be emphasized, however, that, according to the Fe 2p spectra, surface ferrous iron can rather easily oxidize to Fe(III)–S and Fe(III)–O species which release from the lattice into aqueous media or ferric oxyhydroxide phases.

3.2.3.4. Gold uptake and open circuit potentials of minerals. The Au/S ratios obtained from the photoelectron spectra were used to characterize, at least semi-quantitatively, the uptake of gold (Table 1). The ratios steadily increase with the reaction time and strongly depend on the preliminary treatment of pyrite surfaces. The concentration of precipitated gold is lower for a fracture surface; it increases if pyrite was moderately oxidized, in particular, as a result of polishing or exposure to the atmosphere. At the same time, the ferric iron leaching retarded the following reduction of gold. Similar results also were obtained for chalcopyrite and pyrrhotite (Table 1), and previously for arsenopyrite (Mikhlin et al., 2006a), and they are in qualitative agreement with the STM data. It is noteworthy that the non-oxidative acidic leaching of pyrrhotite that produces a very thick, strongly iron-deficient layer (Mikhlin, 2000; Mikhlin et al., 2000; Mikhlin and Tomashevich, 2005) effectively increases the gold uptake.

Comparison of the deposition of gold on the sulfide minerals polished and then reacted under the same conditions (10^{-4} M $HAuCl_4$, pH 1.5, 10 min) revealed that the Au/S ratios increase in the order $Fe_7S_8 < FeS_2 < FeAsS < PbS < ZnS \approx CuFeS_2$. It is interesting to compare this range with

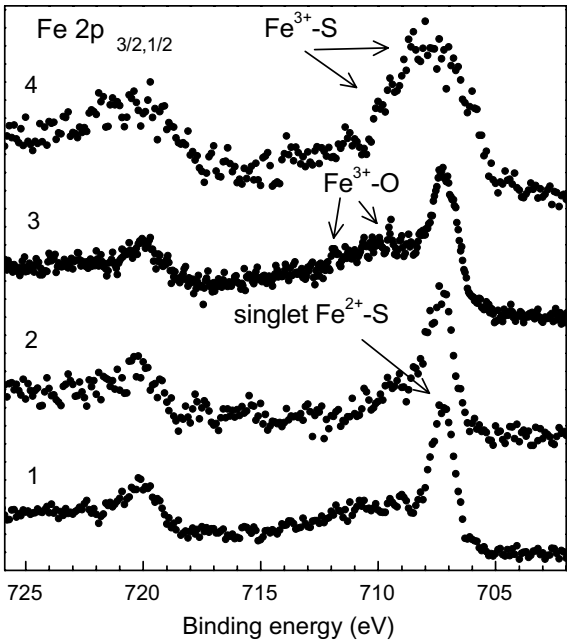

Fig. 11. Fe 2p spectra from pyrite (1) fractured in air, polished and reacted with 10^{-4} M $HAuCl_4$ solution for 10 min (2) at pH 1.5 and (3) pH 3, (4) leached in 0.5 M H_2SO_4 + 0.2 M $Fe_2(SO_4)_3$ at 50 °C for 30 min.

Table 1
Concentrations of gold deposited on minerals as determined by XPS

Mineral samples	Deposition time (min)	Atomic Au/S ratios
Pyrite polished	2	0.055
Pyrite polished	10	0.23
Pyrite polished	30	0.94
Pyrite fractured	10	0.06
Pyrite anodized in a sweep to 1.1 V	5	0.18
Pyrite leached in 0.5 M H_2SO_4 + 0.2 M $Fe_2(SO_4)_3$ for 30 min	30	0.11
Pyrrhotite polished	10	0.07
Pyrrhotite leached in 0.5 M H_2SO_4 for 30 min	10	0.84
Pyrrhotite leached in 0.5 M H_2SO_4 + 0.2 M $Fe_2(SO_4)_3$ for 30 min	10	0.07
Chalcopyrite polished	10	0.66
Chalcopyrite leached in 1 M HCl + 0.4 M $FeCl_3$ for 30 min	10	0.020
Galena polished	10	0.54
Sphalerite polished	10	0.65
Arsenopyrite polished	10	0.41

the open circuit potentials measured after 10 min immersion of polished samples in acidic 10^{-4} M $HAuCl_4$ electrolytes or gold-free, air-saturated 1 M HCl for reference (Table 2). The potentials were not stable and changed with time because the surfaces altered during reaction, and the values should be considered as approximate. The potentials of pyrite, pyrrhotite, and arsenopyrite were more positive

Table 2
Open circuit electrode potentials of polished minerals

Mineral samples	Potentials (V vs Ag/AgCl)		
	1 M HCl	10^{-4} M $HAuCl_4$, pH 0	10^{-4} M $HAuCl_4$, pH 1.5
Pyrite	0.42 ± 0.01	0.52 ± 0.01	0.44 ± 0.02
Pyrrhotite	0.45 ± 0.01	0.46 ± 0.01	0.45 ± 0.02
Arsenopyrite	0.38 ± 0.01	0.48 ± 0.02	0.44 ± 0.02
Chalcopyrite	0.40 ± 0.02	0.35 ± 0.01	0.38 ± 0.01
Galena	0.18 ± 0.02	0.10 ± 0.01	0.20 ± 0.01
Sphalerite	−0.47 ± 0.1	−0.49 ± 0.1	−0.5 ± 0.1

and they became higher in the presence of aqueous gold, whereas the potentials of sphalerite, galena and chalcopyrite were lower and decreased in the Au(III)-bearing solutions. On the whole, one can say that the uptake of gold is roughly larger for minerals having less positive potentials, excluding maybe chalcopyrite.

3.3. Deposition of silver

We performed a series of experiments on the interaction of metal sulfides with a 10^{-4} M $AgNO_3$ solution in order to compare surface silver and gold species produced under comparable conditions. Silver has been reported to form mainly silver sulfide Ag_2S (Price and Warren, 1986; Buckley et al., 1989; Scaini et al., 1997; Barzyk et al., 2002), although photoelectron Ag 5d spectra with Ag $5d_{5/2}$ peak at about 368.2 eV and Ag $M_4N_{45}N_{45}$ Auger spectra (not shown in Figures) do not allow differentiating between metallic silver, Ag_2S and adsorbed silver species reliably. The S 2p spectra of reacted minerals show minimal contributions from polysulfide and substantially increased signals from monosulfide at about 161.4 eV. Moreover, the last component becomes the strongest in the spectra of chalcopyrite and pyrrhotite leached in Fe(III) solutions before the deposition of silver (Fig. 12), suggesting that S–S bonds in polysulfide ions disrupted to form Ag–S bonds instead.

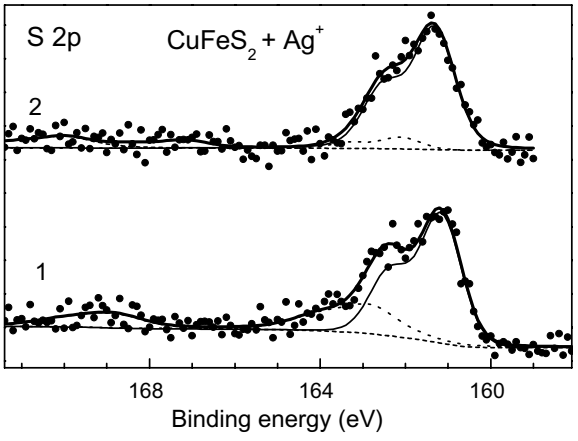

Fig. 12. S 2p spectra from chalcopyrite (1) polished and (2) pretreated in 0.5 M H_2SO_4 + 0.2 M $Fe_2(SO_4)_3$ solution at 50 °C for 30 min and then reacted in 10^{-4} M $AgNO_3$ (pH 6) for 10 min.

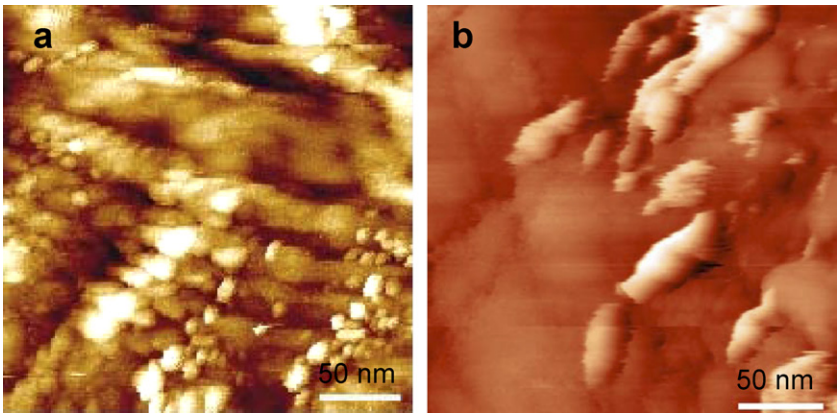

Fig. 13. STM images of (a) pyrite and (b) chalcopyrite reacted in 10^{-4} – M $AgNO_3$ for 10 min.

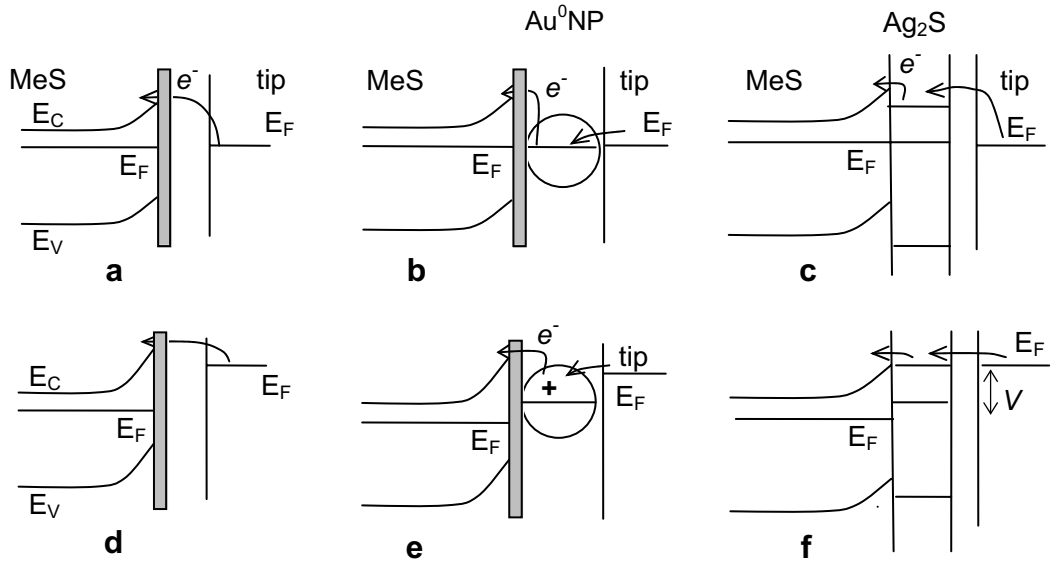

Fig. 14. Scheme of energy levels and electron transitions for (a,d) semiconducting mineral—STM/STS tip, (b and e) mineral–Au^0 NP–tip, and (c,f) mineral–semiconductor (Ag_2S)–tip junctions at (a–c) zero bias and (d–f) a positive voltage V applied to the samples. The plus sign in (e) signifies that, in addition to the potential barrier, the electron transfer is retarded by the positive charge arising at Au NPs.

STM shows an emergence of rounded or slightly elongated particles from 5 to 30 nm in size and, in some occasions, islands of irregular shape; two examples are given in Fig. 13. The tunneling I–V curves measured above the Ag-containing products on different minerals (Fig. 6) represent a widened conductance gap and a sharp current rise at rather high negative or, more often, positive biases. This can be rationalized in terms of a potential barrier between two semiconductors (Fig. 14), more exactly, a model of a planar semiconductor–insulator–semiconductor–insulator–metal structure (Walzer et al., 2003), in which metal stands for a tip, and semiconductors are Ag_2S, which has the gap about 1 eV (Brühwiler et al., 1999, 2002), and an underlying mineral having the gap close to or less than 1 eV. The current sharply increases when the band edge, for instance, of the conduction band of the nanoparticle aligns with that of the semiconductor substrate and the Fermi level of the tip at a positive sample bias (Fig. 14c and f). The behaviour of the system is complicated by band bending, heterogeneity of the oxidized mineral surfaces, etc. It cannot be excluded that intermediate surface products exist between Ag_2S and sulfidic supports, or metallic silver forms above the silver sulfide after large enough exposures, which then oxidizes to silver oxides.

4. DISCUSSION

4.1. Mechanisms for gold deposition

Our experiments show that the deposition of gold on surfaces of sulfide minerals depends upon their nature, exhibiting the range $CuFeS_2 > ZnS > PbS > FeAsS > FeS_2 > Fe_7S_8$ for the minerals polished in air. This somewhat unexpected order does not contradict the previous

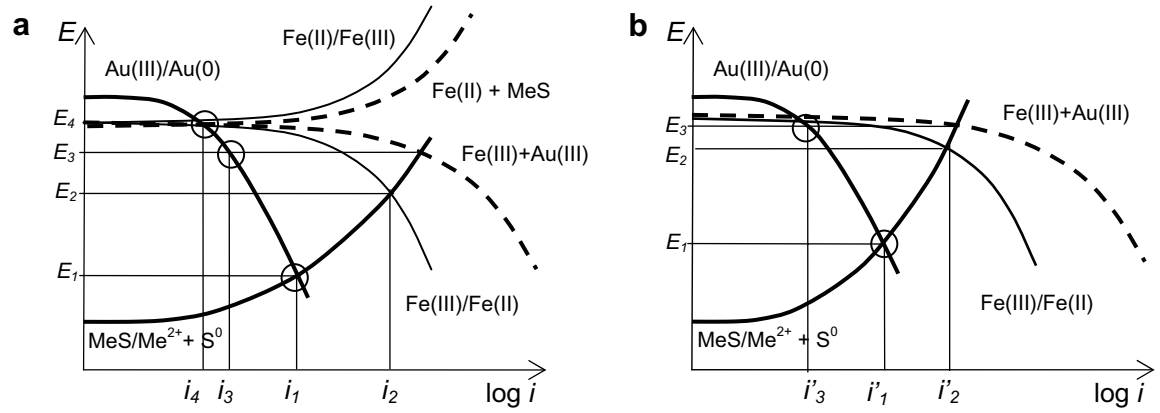

Fig. 15. Schematic anodic and cathodic currents for a sulfide mineral in Au- and Fe-bearing solutions. The mixed potential E_1 and current i_1 correspond to the deposition of gold via the electrochemical mechanism in absence of other redox couples; the potential E_2 and current i_2 relate to the oxidative leaching of metal sulfides in Fe(III)-bearing media. The dashed curves show the total anodic and cathodic currents in the presence of the Fe(III)/Fe(II) couple, and the currents i_3 and i_4 stand for the gold reduction rates at the open circuit potentials E_3 and E_4 in solutions with low and high Fe(II) concentrations, respectively (the equilibrium potential and the exchange current for the reaction $Fe(III) + e \Longleftrightarrow Fe(II)$ are conventionally taken the same for both cases). (b) illustrates the inhibition of the gold deposition due to the slower oxidation of metal sulfide ($i' < i$).

work (Maddox et al., 1998; Mycroft et al., 1995; Scaini et al., 1997; Heasman et al., 2003) and it may be in part due to the surface pre-treatment. It is noteworthy that the lower is content of ferrous iron in a mineral, the higher, with little exceptions, is the uptake of gold. Moreover, the correlation between the gold uptake and open circuit potentials of minerals, i.e. the uptake is larger for minerals having less positive potentials (Table 2), suggests that some inherent mechanisms are involved. Maddox et al. (1998) have previously found the same tendency when comparing the deposition of gold on pyrite and arsenopyrite. This has been explained in terms of the electrochemical mechanism combining the cathodic reduction of gold species and anodic oxidation of the metal sulfides, and the rates (currents) of the coupled half-reactions were considered to be equal. In Fig. 15, this situation is schematically illustrated in solid lines, the intersection of which gives mixed potential E_1 and the current i_1 corresponding to the gold deposition rate. It is commonly known that the mixed potential is closer to the equilibrium potential of a reaction having higher exchange current (compare, for example, the values of E_1 and i_1 in Fig. 15a and b). One may suggest therefore that the deposition of gold on pyrite and pyrrhotite is limited by their oxidation rates to a higher extent than on galena and chalcopyrite under the same conditions. Furthermore, both potentials and photoelectron spectra of metal sulfides reacted in gold-bearing solutions (Section 3.2.3.2) imply that the ability of minerals to host gold changes sympathetically with their oxidability in aqueous solutions.

The above range, however, differs from the usual order of the oxidation rates for metal sulfides. For example, pyrrhotite is one of the most reactive sulfide minerals while chalcopyrite is fairly refractory. The precipitation of gold is also greatly affected by the surface pre-treatment in such a way that moderate oxidation of minerals, usually making them passive, promotes the process. Earlier, Mycroft and co-workers (1995) have reported the enlarged uptake of gold by oxidized surfaces of pyrite, ascribed to a conceivable increase in a number of surface centers for gold nucleation. Mikhlin et al. (2006a) suggested that the reduction of gold on arsenopyrite was facilitated owing to the production of either reducing iron- and arsenic-containing intermediates or passive disordered surface layers of the reacted mineral. These facts scantily agree with the simplistic conclusion that the rate of the Au deposition is controlled mainly by the oxidation of minerals.

One must bear in mind that the systems under investigation contain dissolved oxygen, ferrous and ferric ions, and other species, surface concentrations of which can be higher than those of gold complexes, so the open circuit potentials of metal sulfides are determined in reality by all relevant reactions (Fig. 15). Moreover, the Fe(III)/Fe(II) redox couple is well-known to have high exchange currents, imposing its potential on solid, thus the potentials are expected to be largely controlled by the iron moiety. Au(III)/(I)/(0) species appear to make a small contribution to the total currents and to have a little impact on the mixed potential due to their comparably low concentrations and exchange currents. The reduction of gold is governed by the resulting potential of metal sulfide (E_3 or E_4), and it is faster at more negative (less positive) potentials, as this is shown in Fig. 15. Consequently, the uptake of gold strongly depends upon redox reactants occurring in solutions, first of all Fe(III) and Fe(II) ions, and, finally, upon the content of iron (II) in minerals. The behaviour of Fe(III)/Fe(II) species near the metal sulfide surfaces is complex as Fe(II) is produced via both the reduction of Fe(III) and oxidation of sulfides containing ferrous iron (Nicol and Lázaro, 2002). It also depends on the surface properties of individual minerals; particularly, chalcopyrite exhibits a very low reactivity towards the Fe(III)/Fe(II) couple (Nicol and Lázaro, 2002), probably due to passivation. It is worth to mention that mixed Fe(II)/Fe(III) hydroxides (green rusts) are capable to reduce gold(III) and silver(I) directly, yielding metallic nanoparticles (Heasman et al., 2003; O'Loughlin et al., 2003), but unlikely to contribute substantially to the deposition of gold on metal sulfides.

A question arises how these findings relate to the incorporation of gold into the minerals under natural hydrothermal conditions. Albeit concentrations of "invisible" gold both in natural and synthetic minerals vary in a great range, the data available in the literature rather agree with the results obtained in the current study. Specifically, there is an agreement that the Au contents in pyrites are generally small, except in the arsenian varieties (Cook and Chryssoulis, 1990; Fleet and Mumin, 1997; Tauson, 1999). Cook and Chryssoulis (1990) have concluded that chalcopyrite and galena generally contain minor quantities of "invisible" gold, but maximal concentrations they have found in these minerals (7.7 ppm and 3.4 ppm, respectively) were higher than in pyrrhotite (1.8 ppm) and in a majority of non-arsenian pyrite specimens. Tauson et al. (1996) have established that the concentrations of gold hosted by metal sulfides during hydrothermal synthesis in chloride solutions (500 °C, 1 kbar) comply with the order $FeS_2 < (Zn,Fe)S < Fe_{1-x}S \approx CdS < CuFeS_2 < PbS$, that is similar, with few exceptions, to the one discussed above. Of course, this is not valid for gold forming its own minerals, etc.

Concentrations of hydrosulfide and chloride complexes of gold(I) and especially gold(III) in natural fluids are notably less than in the laboratory experiments (Barnes, 1979), and their influence on the potentials of metal sulfides all the more to be neglected. In that case, the potentials are largely determined by concentrations of soluble redox components, fugacities of H_2, H_2S, and buffering by mineral assemblages. Therefore, the accumulation of gold in As-rich pyrites and arsenopyrite can be explained by the fact that these minerals deposit at lower potentials than non-arsenian pyrite (Pokrovski et al., 2002). This means that arsenic in pyrite just marks the favorable conditions, and there are no structural motives behind the relationship of As and Au. Similar ideas were proposed earlier by Möller and Kersten (1994) and Pokrovski et al. (2002). We should emphasize, however, that the deposition of gold is not simple cathodic reduction but it proceeds via the electrochemical mechanism involving the oxidation of sulfide minerals, possibly local. The admixture of arsenic likely facilitates the oxidation of pyrite and thus the deposition of gold, converting mineral pyrite to p-type conductivity (Mironov et al., 1981). The deficiency of iron in pyrite lattice that is often associated with the incorporation of gold (Fleet and Mumin, 1997) may be not a reason but a result of the oxidation of pyrite. In addition, the solubility of hydrosulfide–chloride complexes of gold strongly depends on the electrochemical potential of the fluids (Laptev and Rozov, 2006). The current study, however, is focused on the surface reaction mechanisms, and other factors determining the formation of gold deposits are not discussed in depth.

4.2. Characteristics of gold nanoparticles

Gold forms mainly metallic nanoparticles, size, shape and spatial distribution of which vary under different conditions. The particles were usually smaller if the total uptake of gold was lower, although on galena they remained less than 10 nm even after significant exposures. Gold islands visualized using SEM were larger (Mycroft et al., 1997; Scaini et al., 1998), but Au^0 nanoparticles discovered in natural arsenian pyrite by TEM (Palenik et al., 2004; Reich et al., 2005) were 5–10 nm, in good accord with the STM data. The nanoparticles appear to be responsible for the Au 4f XPS lines shifted towards higher binding energies as compared with bulk metallic gold. Mycroft et al. (1995), Scaini et al. (1997, 1998), Maddox et al. (1998) have observed similar lines for pyrite, galena, arsenopyrite reacted in Au(III) chloride or Au(I) hydrosulfide solutions but found poor reproducibility and no clear tendency for the peak position, width and intensity. Scaini et al. (1998) proposed that there was a mixture of Au(I) and both small clusters containing less than 100 Au atoms and bulk Au metal on the FeS_2 surface contacted with aqueous Au(I) hydrosulfide. In the present work, the size of gold nanoparticles specified by STM changed sympathetically with the shift of the Au 4f signals, suggesting that the amount of smaller clusters possibly unseen in STM is minor, if any. This implies that the Au NPs have some special properties responsible for the size effects in XPS and STS, which were commonly observed for essentially smaller particles (Han et al., 1998; Daniel and Astruc, 2004; Boyen et al., 2005). The effects take place at semimetallic pyrrhotite, narrow-gap PbS and chalcopyrite, pyrite and arsenopyrite having the gap width about 1 eV, and wide-gap sphalerite, and the peculiarity of the Au NPs may be related either with a character of the gold–sulfide mineral interface, or with sulfur species occurring on or within the gold particles, or with all of these reasons. An isolating film composed of elemental sulfur or/and metal oxyhydroxides can be formed underneath the Au NPs, despite it was not revealed by SPM and SEM for certain. Then, the reacted surface layers of metal sulfide phases are thought to be akin to disordered semiconductors (Mikhlin et al., 2004b, 2006a,b), exhibiting considerably reduced mobility of charge carriers and largely increased impedance (Mott and Davis, 1982; Tsendin et al., 1996). Another important factor is the effect that sulfur seems to exert on gold clusters. Sulfur containing organic molecules are widely used to passivate synthetic Au NPs (Daniel and Astruc, 2004). The reaction of inorganic sulfur species, such as hydrogen sulfide, thiosulfate, and others, with $AuCl_4^-$ complexes produces Au NP sols, which structure and very interesting properties are still poorly studied (Zhou et al., 1994; Schwartzberg et al., 2004; Diao and Chen, 2006). On the surface of bulk gold, sulfur forms very thin, mostly mono- or submonolayer films of gold sulfide Au_2S (and, probably, AuS in vacuum (Quek et al., 2006)), polysulfides, elemental sulfur, and polythionates (Vericat et al., 2004; Woods et al., 2006) at different electrode potentials. Only minimal quantities of Au(I)–S species were found in the current research, suggesting that sulfur most likely forms a thin polysulfide-type layer on gold NPs (Vericat et al., 2004) due to the interaction with hydrosulfide and thiosulfate ions released from corroding sulfide minerals. We suggested that the effects observed both in XPS and STS are mainly caused by temporal electric charging of the nanoparticles, which have small enough capacitance and are electrically isolated from the support (Mikhlin et al., 2006a). Concurrently, sulfur adsorbed on gold NPs may affect the interfacial electron transfer (Geng et al.,

2005), including the electrochemical behaviour of Au NPs (Chen et al., 1998; Chen, 2004; Su and Girault, 2005) and the kinetics of gold deposition and dissolution. Interestingly, the smaller Au particles were observed on galena and pyrrhotite, which release hydrogen sulfide at much faster rates than chalcopyrite and pyrite. In all likelihood, sulfur has some bearing on morphology of precipitating gold by inhibiting the growth of metallic particles (Zweifel and Wei, 2005) and also affecting their association (Geng et al., 2002). We guess that sulfur may play a role in the formation of inner boundaries within rather big gold particles. Although the properties of Au NPs, as well as the Au–mineral interfaces, still need to be examined in detail, the above findings can be, in particular, employed in a procedure of identification of "invisible" gold and silver species in natural systems.

5. CONCLUSIONS

The quantity of gold spontaneously deposited on pyrite increases with reaction time and depends on the surface pre-treatment. Particularly, the concentrations of precipitated gold are lower for fracture surfaces and they increase if the surfaces of pyrite, as well as chalcopyrite, pyrrhotite, galena were moderately oxidized, while the preliminary oxidative leaching in Fe(III)-bearing media retarded the precipitation by many times. For minerals polished in air, the gold uptake decreases in the order $CuFeS_2 > ZnS > PbS > FeAsS > FeS_2 > Fe_7S_8$. It is significant that the content of Fe(II) in minerals and their open circuit (mixed) potentials both in gold-bearing and gold-free solutions change in approximately the same order, excepting chalcopyrite. We have concluded that the potentials of minerals over the gold deposition are determined by Fe(II)/Fe(III) redox reactions rather than the coupled reduction of gold complexes and oxidation of metal sulfides, with the uptake of gold increasing with decreasing electrochemical potential of a mineral. This is expected to be valid also under hydrothermal conditions, so the accumulation of "invisible" gold in arsenopyrite and As-rich pyrites may be explained by lower potentials of these systems.

Gold deposits mainly as metallic nanoparticles tending, especially on pyrite, to form agglomerates. The Au 4f XPS binding energies increase up to 1 eV with decreasing size of Au^0 nanoparticles in the range 3–20 nm. This was attributed to a temporal charging of the particles, lessening kinetic energies of the photoelectrons via interaction with final-state photoholes. Concurrently, STS revealed a positive correlation between the current magnitude and the diameter of Au particles, tentatively explained by mainly electrostatic phenomena (Coulomb blockade). Silver deposited on the minerals exhibits neither shifts of Ag 5d bands, nor Coulomb blockade in STS. The size effects observed at unusually big gold nanoparticles suggest specific properties of the gold deposited on metal sulfides; they are probably due to the nature of mineral–gold interfaces or/and sulfur species adsorbed on Au NPs. The phenomena can play an important role in the reactivity of "invisible" gold, including the growth of the particles, and they should be taken into account when looking for "invisible" gold in natural materials by means of scanning probe microscopy and XPS.

ACKNOWLEDGMENTS

This work was supported by Interdisciplinary Grant No. 96 of SB RAS, Grant No. 5487.2006.3 for Leading Research Schools of RF, and the bilateral program "Russian–German Laboratory at BESSY". We thank Prof. R. Szargan (Leipzig University) for encouragement and valuable comments, and Dr. L. Makhova (Leipzig University), the staff of BESSY II and the Russian–German Laboratory for their assistance with the SR-XPS experiment. The authors are thankful to Dr. J. Rustad (Associated Editor), Dr. W. Barzyk and the anonymous referees for valuable suggestions to improve the manuscript.

APPENDIX A. SUPPLEMENTARY DATA

Supplementary data associated with this article can be found, in the online version, at doi:10.1016/j.gca.2007.10.001.

REFERENCES

Barnes H. L. (1979) *Geochemistry of Hydrothermal Ore Deposits*. Wiley, New York.

Barzyk W., Kowal A. and Pomianowski A. (2002) Noble metal (Ag, Au) cementation on non-stoichiometric cuprous sulphide grains. *Coll. Surf. A* **208**, 321–335.

Becker U., Vaughan D. J. and Hochella, Jr., M. F. (1997) The adsorption of gold to galena surfaces: calculation of adsorption/reduction energies, reaction mechanisms, XPS spectra, and STM images. *Geochim. Cosmochim. Acta* **61**, 3565–3585.

den Besten J., Jamieson D. N. and Ryan C. G. (1999) Lattice location of gold in natural pyrite crystals. *Nucl. Instrum. Meth. B* **152**, 135–144.

Boyen H.-G., Ethirajan A., Kästle G., Weigl F., Ziemann P., Schmid G., Garnier M. G., Büttner M. and Oelhafen P. (2005) Alloy formation of supported gold nanoparticles at their transition from clusters to solids: does size matter? *Phys. Rev. B* **94**, 016804.

Briggs, D. and Seath, M. P. (1992). Practical surface analysis. V.1, 2nd edition,Wiley, New York.

Brühwiler D., Seifert R. and Calzaferri G. (1999) Quantum-sized silver sulfide clusters in zeolite A. *J. Phys. Chem. B* **103**, 6397–6399.

Brühwiler D., Leiggener C., Glaus S. and Calzaferri G. (2002) Luminescent silver sulfide clusters. *J. Phys. Chem. B* **106**, 3770–3777.

Buckley A. N., Wouterlood H. J. and Woods R. (1989) The interaction of pyrite with solutions containing silver ions. *J. Appl. Electrochem.* **19**, 744–751.

Cabri L. J., Newville M., Gordon R. A., Crozier E. D., Sutton S. R., McMahon G. and Jiang D.-T. (2000) Chemical speciation of gold in arsenopyrite. *Can. Mineral.* **38**, 1265–1281.

Chen S. (2004) Chemical manipulations of nanoscale electron transfers. *J. Electroanal. Chem.* **574**, 153–165.

Chen S., Ingham R. S., Hostetler M. J., Pietron J. J., Murray R. W., Schaaff T. G., Khoury J. T., Alvarez M. M. and Whetten R. L. (1998) Gold nanoelectrodes of varied size: transition to molecule-like charging. *Science* **280**, 2098–2101.

Compagnini G., Scalisi A. A. and Puglisi O. (2006) Spectroscopic characterization of core and shell regions in monolayer protected gold nanoparticles. *Surf. Sci.* **600**, L1–L5.

Cook N. J. and Chryssoulis S. L. (1990) Concentrations of "invisible gold" in the common sulfides. *Can. Mineral.* **28**, 1–16.

Daniel M.-C. and Astruc D. (2004) Gold nanoparticles: assembly, supramolecular chemistry, quantum size-related properties, and applications toward biology, catalysis, and nanotechnology. *Chem. Rev.* **104**, 293–346.

De Guidici G. and Zuddas P. (2001) In situ investigation of galena dissolution in oxygen saturated solution: evolution of surface features and kinetic rate. *Geochim. Cosmochim. Acta* **65**, 1381–1389.

De Guidici G., Voltolini M. and Moret M. (2002) Microscopic surface processes observed during the oxidative dissolution of sphalerite. *Eur. J. Mineral.* **14**, 757–762.

Descostes M., Vitorge P. and Beaucaire C. (2004) Pyrite dissolution in acidic media. *Geochim. Cosmochim. Acta* **68**, 4559–4569.

Diao J. J. and Chen H. (2006) Near infrared surface plasmon resonance of gold tabular nanostructures in the $HAuCl_4$–Na_2S reaction. *J. Chem. Phys.* **124**, 116103.

Eggleston C. M. and Hochella, Jr., M. F. (1991) Scanning tunneling microscopy of galena surface oxidation and sorption of aqueous gold. *Science* **254**, 983–986.

Eggleston C. M. and Hochella, Jr., M. F. (1993) Tunneling spectroscopy applied to PbS (100) surfaces: fresh surfaces, oxidation and sorption of aqueous gold. *Am. Mineral.* **78**, 877–883.

Eggleston C. M. and Hochella, Jr., M. F. (1992) Scanning tunneling microscopy of pyrite {100}: surface structure and step reconstruction. *Am. Mineral.* **77**, 221–224.

Eggleston C. M., Ehrhardt J.-J. and Stumm W. (1996) Surface structural controls on pyrite oxidation kinetics: An XPS-UPS, STM, and modeling study. *Am. Mineral.* **81**, 1036–1056.

Elsetinow A. R., Guevremont J. M., Strongin D. R., Schoonen M. A. A. and Strongin M. (2000) Oxidation of {100} and {111} surfaces of pyrite: effects of preparation method. *Am. Mineral.* **85**, 623–626.

Eyert V., Höck K.-H., Fiechter S. and Tributsch H. (1998) Electronic structure of FeS_2: the crucial role of electron–lattice interaction. *Phys. Rev. B* **57**, 6350–6359.

Fedoseenko S. I., Vyalikh D. V., Iossifov I. E., Follath R., Gorovikova S. A., Püttner R., Schmidt J.-S., Molodtsov S. L., Adamchuk V. K., Gudat W. and Kaindl G. (2003) Commissioning results and performance of the high-resolution Russian–German Beamline at BESSY II. *Nucl. Instrum. Meth. A* **505**, 718–728.

Fleet M. E. and Mumin A. H. (1997) Gold-bearing arsenian pyrite and marcasite and arsenopyrite from Carlin Trend gold deposits and laboratory synthesis. *Am. Mineral.* **82**, 182–193.

Friedl J., Wagner F. E. and Wang N. (1995) On the chemical state of combined gold in sulfidic ores: conclusions from Mössbauer source experiments. *Neues Jahrb Mineral.-Abh.* **169**, 279–290.

Geng J., Johnson B. F. G., Thomas M. D. R., Shephard D. S. and Jiang L. (2002) Behaviour of two-dimensional arrays of gold nanoparticles under H_2S: agglomeration and regeneration. *Inorg. Chim. Acta* **330**, 33–37.

Geng J., Thomas M. D. R., Shephard D. S. and Johnson B. F. G. (2005) Suppressed electron hopping in a Au nanoparticle/H_2S system: development towards a H_2S nanosensor. *Chem. Commun.* **14**, 1895–1897.

Genkin A. D., Bortnikov N. S., Cabri L. J., Wagner F. E., Stanley C. J., Safonov Y. G., McMahon G., Friedl J., Kerzin A. L. and Gamyanin G. N. (1998) A multidisciplinary study of invisible gold in arsenopyrite from four mesothermal gold deposits in Siberia, Russian Federation. *Econ. Geol.* **93**, 463–487.

Hallmeier K. H., Uhlig I. and Szargan R. (2002) Sulphur $L_{2,3}$ and L_1 XANES investigations of pyrite and marcasite. *J. Electron Spectrosc. Rel. Phenom.* **122**, 91–96.

Han M. Y., Zhou L., Quek C. H., Li S. F. Y. and Huang W. (1998) Room temperature Coulomb staircase on pure and uniform surface-capped gold nanoparticles. *Chem. Phys. Lett.* **287**, 47–52.

Heasman D. M., Sherman D. M. and Ragnarsdottir K. V. (2003) The reduction of aqueous Au^{3+} by sulfide minerals and green rust phases. *Am. Mineral.* **88**, 725–738.

Hyland M. M. and Bancroft G. M. (1989) An XPS study of gold deposition at low temperatures on sulphide minerals: reducing agents. *Geochim. Cosmochim. Acta* **53**, 367–372.

Jean G. E. and Bancroft G. M. (1985) An XPS and SEM study of gold deposition at low temperatures on sulphide mineral surfaces: concentration of gold by adsorption/reduction. *Geochim. Cosmochim. Acta* **49**, 979–987.

Kendelewicz T., Doyle C. S., Bostick B. C. and Brown G. E. r. (2004) Initial oxidation of fractured surfaces of FeS_2(100) by molecular oxygen, water vapor, and air. *Surf. Sci.* **558**, 80–88.

Laptev Yu. V. and Rozov K. B. (2006) Interaction of gold with sulfide surface as a factor of its concentration in hydrothermal ore formation. *Dokl. Earth Sci.* **411**, 1229–1232.

Leiro J. A., Mattila S. S. and Laajalehto K. (2003) XPS study of the sulphur 2p spectra of pyrite. *Surf. Sci.* **547**, 157–161.

Lopez-Salido I., Lim D. C., Dietsche R., Bertram N. and Kim Y. D. (2006) Electronic and geometric properties of Au nanoparticles on highly ordered pyrolytic graphite (HOPG) studied using X-ray photoelectron spectroscopy (XPS) and scanning tunneling microscopy (STM). *J. Phys. Chem. B* **110**, 1128–1136.

Maddox L. M., Bancroft G. M., Scaini M. J. and Lorimer J. W. (1998) Invisible gold: comparison of Au deposition on pyrite and arsenopyrite. *Am. Mineral.* **83**, 1240–1245.

Mikhlin Yu. (2000) Reactivity of pyrrhotite surfaces: an electrochemical study. *Phys. Chem. Chem. Phys.* **2**, 5672–5677.

Mikhlin Yu., Varnek V., Asanov I., Tomashevich Ye., Okotrub A., Livshits A., Selyutin G. and Pashkov G. (2000) Reactivity of pyrrhotite (Fe_9S_{10}) surfaces: spectroscopic studies. *Phys. Chem. Chem. Phys.* **2**, 4393–4398.

Mikhlin Yu., Kuklinskiy A., Mikhlina E., Kargin V. and Asanov I. (2004a) Electrochemical behaviour of galena (PbS) in aqueous nitric acid and perchloric acid solutions. *J. Appl. Electrochem.* **34**, 37–46.

Mikhlin Yu. L., Tomashevich Ye. V., Asanov I. P., Okotrub A. V., Varnek V. A. and Vyalikh D. V. (2004b) Spectroscopic and electrochemical characterization of the surface layers of chalcopyrite ($CuFeS_2$) reacted in acidic solutions. *Appl. Surf. Sci.* **225**, 395–409.

Mikhlin Yu. and Tomashevich Ye. (2005) Pristine and reacted surfaces of pyrrhotite and arsenopyrite as studied by X-ray absorption near-edge structure spectroscopy. *Phys. Chem. Minerals* **32**, 19–27.

Mikhlin Yu., Romanchenko A. and Asanov I. (2006a) Oxidation of arsenopyrite and deposition of gold on the oxidized surfaces: a scanning probe microscopy, tunneling spectroscopy, and XPS study. *Geochim. Cosmochim. Acta* **70**, 4874–4888.

Mikhlin Yu., Romanchenko A. and Shagaev A. (2006b) Scanning probe microscopy studies of PbS surfaces oxidized in air and etched in aqueous acid solutions. *Appl. Surf. Sci.* **252**, 5245–5258.

Mironov A. G., Zhodik S. M. and Maksimova E. A. (1981) An experimental investigation of the sorption of gold by pyrites with different thermoelectric properties. *Geochem. Int.* **18**, 153–160.

Möller P. and Kersten G. (1994) Electrochemical accumulation of visible gold on pyrite and arsenopyrite surfaces. *Miner. Deposita* **29**, 404–413.

Mott N. F. and Davis E. A. (1979) *Electron Processes in Noncrystalline Materials*. Clarendon Press, Oxford.

Mycroft J. R., Bancroft G. M., McIntyre N. S. and Lorimer J. W. (1995) Spontaneous deposition of gold on pyrite from solution containing Au(III) and Au(I) chlorides: part I, a surface study. *Geochim. Cosmochim. Acta* **59**, 3351–3365.

Nesbitt H. W., Bancroft G. M., Pratt A. R. and Scaini M. J. (1998) Sulfur and iron surface states on fractured pyrite surfaces. *Am. Mineral.* **83**, 1067–1076.

Nesbitt H. W., Scaini M., Hoechst H., Brancroft G. M., Schaufuss A. G. and Szargan R. (2000) Synchrotron XPS evidence for Fe^{2+}–S and Fe^{3+}–S surface species on pyrite fracture surfaces and their 3d electronic states. *Am. Mineral.* **85**, 850–857.

Nicol M. J. and Lázaro I. (2002) The role of E_H measurements in the interpretation of the kinetics and mechanisms of the oxidation and leaching of sulphide minerals. *Hydrometallurgy* **63**, 15–22.

Ohgi T. and Fujita D. (2003) Single electron charging effects in gold nanoclusters on alkanedithiol layers with different molecular lengths. *Surf. Sci.* **532–535**, 294–299.

O'Loughlin E. J., Kelly S. D., Kemner K. M., Csencsits R. and Cook R. E. (2003) Reduction of Ag^{I}, Au^{III}, Cu^{II}, and Hg^{II} by Fe^{II}/Fe^{III} hydroxysulfate green rust. *Chemosphere* **53**, 437–446.

Okazawa T., Fujiwara M., Nishimura T., Akita T., Kohyama M. and Kido Y. (2006) Growth mode and electronic structure of Au nano-clusters on NiO(0 0 1) and TiO_2(1 1 0). *Surf. Sci.* **600**, 1331–1338.

Palenik C. S., Utsunomiya S., Reich M., Kesler S. E., Wang L. and Ewing R. C. (2004) "Invisible" gold revealed: direct imaging of gold nanoparticles in a Carlin-type deposit. *Am. Mineral.* **89**, 1359–1366.

Pokrovski G. S., Kara S. and Roux J. (2002) Stability and solubility of arsenopyrite, FeAsS, in crustal fluids. *Geochim. Cosmochim. Acta* **66**, 2361–2378.

Price D. W. and Warren G. W. (1986) The influence of silver ion on the electrochemical response of chalcopyrite and other mineral sulfide electrodes in sulfuric acid. *Hydrometallurgy* **15**, 303–324.

Quek S. Y., Biener M. M., Biener J., Bhattacharjee J., Friend C. M., Waghmare U. V. and Kaxiras E. (2006) Rich coordination chemistry of Au adatoms in gold sulfide monolayer on Au(1 1 1). *J. Phys. Chem. B* **110**, 15663–15665.

Reich M., Kesler S. E., Utsunomiya S., Palenik C. S., Chryssoulis S. L. and Ewing R. C. (2005) Solubility of gold in arsenian pyrite. *Geochim. Cosmochim. Acta* **69**, 2781–2796.

Richter B., Kuhlenbeck H., Freund H.-J. and Bagus P. S. (2004) Cluster core-level binding energy shifts: the role of lattice strain. *Phys. Rev. Lett.* **93**, 026805(4).

Rimstidt J. D. and Vaughan D. J. (2003) Pyrite oxidation: a state-of-the-art assessment of the reaction mechanism. *Geochim. Cosmochim. Acta* **67**, 873–880.

Rosso K. M., Becker U. and Hochella, Jr., M. F. (1999) The interaction of pyrite {1 0 0} surfaces with O_2 and H_2O: fundamental oxidation mechanisms. *Am. Mineral.* **84**, 1549–1561.

Rosso K. M., Becker U. and Hochella, Jr., M. F. (2000) Surface defects and self-diffusion on pyrite {1 0 0}: an ultra-high vacuum scanning tunneling microscopy and theoretical modeling study. *Am. Mineral.* **85**, 1428–1436.

Rosso K. M. and Vaughan D. J. (2006a) Sulfide mineral surfaces. *Rev. Mineral. Geochem.* **61**, 505–556.

Rosso K. M. and Vaughan D. J. (2006b) Reactivity of sulfide mineral surfaces. *Rev. Mineral. Geochem.* **61**, 505–556.

Sakharova M. S., Batrakova Yu. A. and Ryakhovskaya S. K. (1975) Investigation of electrochemical interactions between sulphides and Au bearing-solutions. *Trans. Geokhimiya* **5**, 740–745.

Scaini M. J., Bancroft G. M. and Knipe S. W. (1997) An XPS, AES, and SEM study of the interactions of gold and silver chloride species with PbS and FeS_2: comparison to natural samples. *Geochim. Cosmochim. Acta* **61**, 1223–1231.

Scaini M. J., Bancroft G. M. and Knipe S. W. (1998) Reactions of aqueous Au^{1+} sulfide species with pyrite as a function of pH and temperature. *Am. Mineral.* **83**, 316–322.

Schaufuss A. G., Nesbitt H. W., Kartio I., Laajalehto K., Bancroft G. M. and Szargan R. (1998a) Reactivity of surface chemical states on fractured pyrite. *Surf. Sci.* **411**, 321–328.

Schaufuss A. G., Nesbitt H. W., Kartio I., Laajalehto K., Bancroft G. M. and Szargan R. (1998b) Incipient oxidation of fractured pyrite surfaces in air. *J. Electron Spectrosc. Related Phenom.* **96**, 69–82.

Schwartzberg A. M., Grant C. D., Wolcott A., Talley C. E., Huser T. R., Bogomolni R. and Zhang J. Z. (2004) Unique gold nanoparticle aggregates as a highly active surface-enhanced Raman scattering substrate. *J. Phys. Chem. B* **108**, 19191–19197.

Simon G., Huang H., Penner-Hahn J. E., Kesler S. E. and Kao Li-Shu (1999a) Oxidation state of gold and arsenic in gold-bearing arsenian pyrite. *Am. Mineral.* **84**, 1071–1079.

Simon G., Kesler S. E. and Chryssoulis S. L. (1999b) Geochemistry and textures of gold-bearing arsenian pyrite, Twin Creeks Carlintype gold deposit, Nevada. Implications for gold deposition. *Econ. Geol.* **94**, 405–422.

Su B. and Girault H. H. (2005) Redox properties of self-assembled gold nanoclusters. *J. Phys. Chem. B* **109**, 23925–23929.

Tanaka A., Takeda Y., Imamura M. and Sato S. (2003) Dynamic finalstate effect on the Au 4f core-level photoemission of dodecanethiolate-passivated Au nanoparticles on graphite substrates. *Phys. Rev. B* **68**, 195415.

Tauson V. L. (1999) Gold solubility in the common gold-bearing minerals: experimental evaluation and application to pyrite. *Eur. J. Miner.* **11**, 937–947.

Tauson V. L., Mironov A. G., Smagunov N. V., Bugaeva N. G. and Akimov V. V. (1996) Gold in sulfides: state of the art of occurrence and horizons of experimental studies. *Russ. Geol. Geophys.* **37**, 1–11.

Tauson V. L., Pastushkova T. M. and Bessarabova O. I. (1998) On limit concentration and manner of incorporation of gold in hydrothermal pyrite. *Russ. Geol. Geophys.* **39**, 932–940.

Termes S. C., Buckley A. N. and Gillard R. D. (1987) 2p electron binding energies for the sulfur atoms in metal polysulphides. *Inorg. Chim. Acta* **126**, 79–82.

Todd E. C., Sherman D. M. and Purton J. A. (2003) Surface oxidation of pyrite under ambient atmospheric and aqueous (pH = 2 to 10) conditions: electronic structure and mineralogy from X-ray absorption spectroscopy. *Geochim. Cosmochim. Acta* **67**, 881–893.

Tsendin, K. D. (ed.) (1996) *Electron Phenomena in Chalcogenide Glassy Semiconductors*. Nauka, St. Peterburg.

Uhlig I., Szargan R., Nesbitt H. W. and Laajalehto K. (2001) Surface states and reactivity of pyrite and marcasite. *Appl. Surf. Sci.* **17**, 222–229.

Vericat C., Vela M. E., Gago J. and Salvarezza R. C. (2004) Sulfur electroadsorption on Au(1 1 1). *Electrochim. Acta* **49**, 3643–3649.

Walzer K., Marx E., Greenham N. C. and Stokbro K. (2003) Scanning tunneling spectroscopy of CdSe nanocrystals covalently bound to GaAs. *Surf. Sci.*, 795–800.

Widler A. M. and Seward T. M. (2002) The adsorption of gold(I) hydrosulphide complexes by iron sulphide surfaces. *Geochim. Cosmochim. Acta* **66**, 383–402.

Woods R., Hope G. A., Watling K. M. and Jeffrey M. I. (2006) A spectroelectrochemical study of surface species formed in the gold/thiosulfate system. *J. Electrochem. Soc.* **153**, D105–D113.

Zhou H. S., Honma L. and Koiyama H. (1994) Controlled synthesis and quantum-size effect in gold-coated nanoparticles. *Phys. Rev. B* **50**, 12052–12056.

Zweifel D. A. and Wei A. (2005) Sulfide-arrested growth of gold nanorods. *Chem. Mater.* **17**, 4256–4261.

Associate editor: James R. Rustad